

Microscopic evidence for spin-spinless stripe order with reduced Ni moments within ab plane for bilayer nickelate $\text{La}_3\text{Ni}_2\text{O}_7$ probed by ^{139}La -NQR

Mitsuharu Yashima¹, Nina Seto¹, Yujiro Oshita¹, Masataka Kakoi^{1,2},

Hiroya Sakurai³, Yoshihiko Takano³, and Hidekazu Mukuda¹

¹Graduate School of Engineering Science, Osaka University, Toyonaka, Osaka 560-8531, Japan

²Department of Physics, Osaka University, Toyonaka, Osaka 560-0043, Japan and

³National Institute for Materials Science (NIMS), Tsukuba, Ibaraki 305-0047, Japan

(Dated: March 17, 2025)

The intrinsic electronic properties of $\text{La}_3\text{Ni}_2\text{O}_7$ have been selectively investigated by nuclear quadrupole resonance (NQR) at the $\text{La}(2)$ site outside the NiO_2 bilayers. The $\text{La}(2)_a$ site of the ideal $\text{La}_3\text{Ni}_2\text{O}_7$ is clearly distinguished from the $\text{La}(2)_b$ site close to the local defects. Below 150K, almost half of the intrinsic $\text{La}(2)_a$ sites are dominated by a finite internal field within the ab plane, while the other half are dominated by zero internal field. The result is fully consistent with the single spin-spinless stripe order of $(\cdots \uparrow \circ \downarrow \circ \uparrow \circ \cdots)$, where the reduced Ni magnetic moments are parallel to the ab -plane. Even for the $\text{La}(2)_b$ site, the result is also explained within the same model by considering the inhomogeneous internal magnetic fields enhanced around the nearby defects such as oxygen vacancies. These findings provide unambiguous microscopic evidence for the single spin-spinless stripe order below 150 K at ambient pressure.

1. Introduction

Remarkably high- T_c superconductivity (SC) with a maximum T_c of about 80 K was reported for bilayer nickelate $\text{La}_3\text{Ni}_2\text{O}_{7+\delta}$ (La327) under high pressure in 2023.^{1–6} Since the formal valence of Ni is equivalent to $\text{Ni}^{2.5+}$ ($d^{7.5}$), the $3d_{x^2-y^2/3z^2-r^2}$ orbitals are partially occupied by 1.5 electrons. Thus, multiple degrees of freedom of spin/charge/orbital states in d electrons are expected to play some essential roles for the emergence of SC phase under high pressure. In previous studies on La327($\delta \sim 0$) at ambient pressure, the anomalies in electronic states below 100 \sim 200 K has been reported, suggesting the existence of spin density wave (SDW) and/or charge density wave (CDW).^{2–4,7–19} As possible candidates, the single spin-charge (spin-spinless) stripe order and the double spin stripe order have been proposed from the spectroscopies such as RIXS,¹¹ μSR ,^{15,16} NMR,¹⁹ and RXS,^{17,18} although the static magnetic order has not yet been reported by neutron scattering experiment.²⁰ A dual nature of electrons with spin and charge degrees of freedom may give rise to the complicated states associated with possible defects such as oxygen vacancies (O_{vac} s) and stacking faults. It is highly desirable to determine the intrinsic magnetic and electronic properties of La327 by carefully distinguishing the extrinsic effects due to the defects. In the La327 crystal there are two crystallographically inequivalent La sites, one being La(1) between the NiO_2 planes and the other being La(2) outside the NiO_2 bilayers. Nuclear quadrupole resonance (NQR) provides a unique opportunity to selectively probe the local electronic states at La(1) and La(2) sites, since each NQR frequency (ν_Q) was deduced to be ~ 5.6 (2.2) MHz for the La(2) (La(1)) site.^{5,13,19,21} In this Letter, we report the $^{139}\text{La}(2)$ -NQR study on La327($\delta \sim 0$), which provides unambiguous microscopic evidence for the single spin-spinless stripe order for the ideal crystal site below $T^* \sim 150\text{K}$.

2. Experimental

Polycrystalline La327 ($\delta \sim 0$) was prepared by the solid state reaction method described elsewhere.²² X-ray diffraction ensures a single phase of the orthorhombic structure of La327 ($\delta \sim 0$) with lattice parameters $a = 5.3920\text{\AA}$, $b = 5.4510\text{\AA}$, and $c = 20.533\text{\AA}$.²² The oxygen deficiency δ is determined by thermogravimetric analysis.²² The ^{139}La -NQR study was performed using a coarse powder of La327 ($\delta \sim 0$). For comparison, it was also carried out on the oxygen-deficient polycrystals La327 ($\delta \sim -0.03$)²³ and $\text{La}_4\text{Ni}_3\text{O}_{9.89}$ (La4310)²⁴ synthesized by the different methods. The energy levels of the ^{139}La nuclear spins ($I = 7/2$) are split into four levels ($m = \pm 1/2, \pm 3/2, \pm 5/2, \pm 7/2$) by the nuclear quadrupole interaction, and thus three resonance peaks are observed for each La site in the NQR spectrum. Here, the NQR frequency for the La(i) is defined by $\nu_Q^{(i)} = 3eQV_{zz}^{(i)}/[2I(2I-1)\hbar]$, where $V_{zz}^{(i)}$ is a principal value of the electric field gradient (EFG) tensor at the La(i) site, and Q is the electric quadrupole moment of ^{139}La . The asymmetry parameter of the EFG $\eta^{(i)}$ is defined as $|V_{xx}^{(i)} - V_{yy}^{(i)}|/V_{zz}^{(i)}$. The $^{139}\text{La}(2)$ -NQR spectrum was obtained at zero external field, focusing on the resonances at $2\nu_Q$ ($\pm 5/2 \leftrightarrow \pm 3/2$) and $3\nu_Q$ ($\pm 7/2 \leftrightarrow \pm 5/2$). The nuclear spin relaxation rate ($1/T_1$) was measured at $3\nu_Q$ by the saturation recovery method²⁵.

3. Results

In a perfect crystal of La327 without any defects, we expect only one resonance peak from a single La(2) site in the NQR ($3\nu_Q$) spectrum above $T^* \sim 150\text{K}$ in the paramagnetic state. However, as shown in Fig. 1(a), even in La327 ($\delta \sim 0$), two distinct peaks are observed, labeled $\text{La}(2)_a$ and $\text{La}(2)_b$. The result is compared with

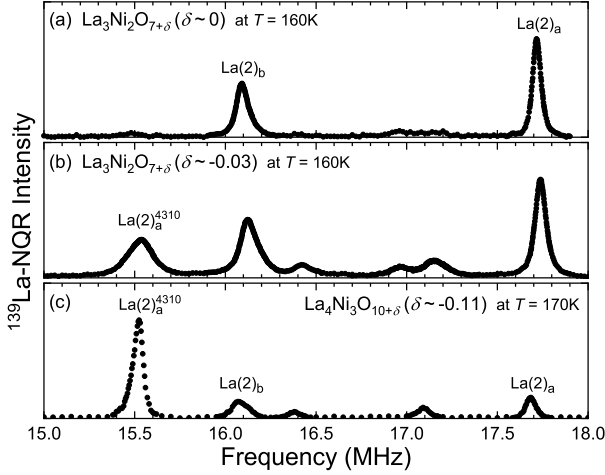


FIG. 1. (Color online) (a) NQR spectra at $3\nu_Q$ of La(2) above T^* in (a) La327 ($\delta \sim 0$), compared to the results in (b) La327 ($\delta \sim -0.03$) and (c) La4310. In La327 ($\delta \sim 0$), two peaks, La(2)_a and La(2)_b, are derived from the site of the ideal La327 and the one near O_{vac} at the inner apical site, respectively. The peak at ~ 15.5 MHz is the intrinsic La(2) site of La4310. The La327 ($\delta \sim 0$) sample in this study contains almost no stacking faults of La4310.

the typical oxygen-deficient sample La327 ($\delta \sim -0.03$) in Fig. 1(b) and La4310 in Fig. 1(c). The peak of La(2)_a has the largest intensity with the narrowest linewidth in both La327 samples, and thus La(2)_a is assigned to the intrinsic La(2) site in the ideal La327 crystal without nearby defects. As for La4310, the largest peak with a narrow linewidth at ~ 15.5 MHz is assigned to the La(2)_a⁴³¹⁰ site of the ideal La4310 crystal without nearby defects. We emphasize that the La327 ($\delta \sim 0$) sample contains almost no stacking faults of La4310.

Next we consider the origin of the La(2)_b site in La327 ($\delta \sim 0$). From the analysis of the $2\nu_Q$ - and $3\nu_Q$ -spectra, we evaluate $\nu_Q^b = 5.422$ MHz and $\eta^b = 0.155$ for La(2)_b at $T = 160$ K, which differ from the values $\nu_Q^a = 5.952$ MHz and $\eta^a = 0$ for La(2)_a. As shown in Fig. 2(a), the T dependence of the $3\nu_Q$ -peak frequency at La(2)_b is quite similar to that at La(2)_a above T^* . This indicates that they both belong to the same crystalline unit, which has almost the same T dependence of the local EFG derived from the thermal shrinkage of the lattice. Furthermore, as shown in Fig. 2(b), the T dependence of $(T_1 T)^{-1}$ at La(2)_b is exactly the same as that at La(2)_a, although these absolute values are about 10 times different. In general, $(T_1 T)^{-1}$ is proportional to $|A_{\text{hf}}^{\text{a,b}}|^2 \chi''(q, \omega)$, where $A_{\text{hf}}^{\text{a,b}}$ is a hyperfine coupling constant at each La(2) site, and $\chi''(q, \omega)$ is a dynamical spin susceptibility. The identical T dependences of $(T_1 T)^{-1}$ are attributed to the $\chi''(q, \omega)$ coming from NiO₂ bilayers in common. Thus, the difference in the absolute values of $(T_1 T)^{-1}$ is mostly attributed to that in $A_{\text{hf}}^{\text{a,b}}$, which allows us to obtain the ratio $|A_{\text{hf}}^b/A_{\text{hf}}^a| \sim 3.06$ from $[(T_1 T)_b^{-1}/(T_1 T)_a^{-1}]^{0.5}$. Considering these experimental facts, we assigned La(2)_b to the La(2) site near an O_{vac} .

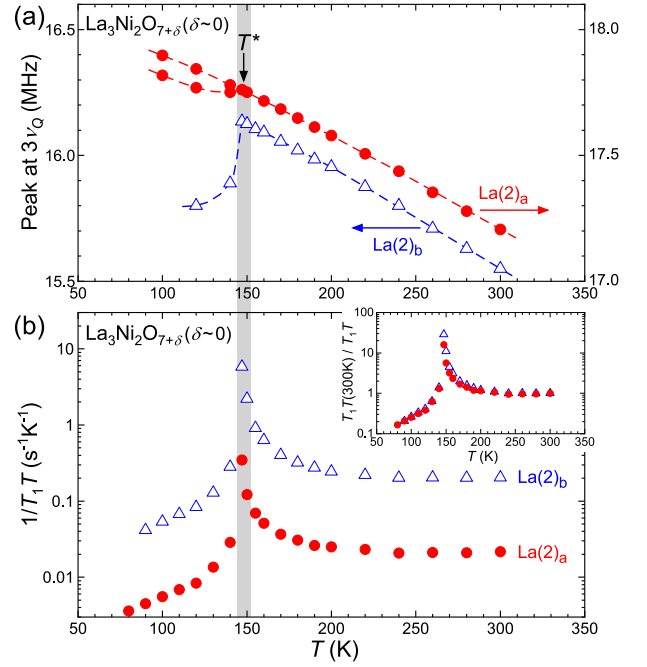


FIG. 2. (Color online) T -dependences of (a) peak frequencies at $3\nu_Q$ and (b) $(T_1 T)^{-1}$ for La(2)_a and La(2)_b of La327 ($\delta \sim 0$). The inset of (b) shows the identical T dependences of $(T_1 T)^{-1}$ normalized by the values at $T = 300$ K for La(2)_a and La(2)_b.

It has been reported that most of O_{vac} s exist at an inner apical site between NiO₂ planes.²⁶ The inner apical O_{vac} probably induces the anisotropy and inhomogeneity of EFG at the La(2)_b site, which has the finite η^b ($= 0.155$) and the broader linewidth than that of La(2)_a for each sample. In addition, the presence of O_{vac} gives a local distortion to its surrounding space and induces a change in the hybridization between Ni and La(2), probably leading to the modulation of A_{hf} at La(2) transferred from nearby Ni sites.

Next we focus on the spin/charge ordered states below T^* at La(2)_a for La327 ($\delta \sim 0$). Figure 3(a) shows the T variations of the $2\nu_Q$ - and $3\nu_Q$ -spectra across T^* . As for La(2)_a, the $2\nu_Q$ -spectrum around 11.9 MHz is largely split into three peaks below T^* , where two broad peaks shift to the lower frequencies, while the other one with a narrow linewidth remains around the frequency corresponding to zero internal field. In contrast, the $3\nu_Q$ -spectrum at ~ 17.8 MHz shows a slight splitting into two narrow peaks. The $1/T_1$ values measured at all these peaks are almost the same, ruling out the possibility of phase separation. Furthermore, it cannot be attributed to the charge anomaly primarily: considering the relation $\nu_Q \propto V_{zz}$, the deformation of the $3\nu_Q$ -spectrum should be ~ 1.5 times larger than that of the $2\nu_Q$ -spectrum if the charge anomaly such as CDW is a primary cause. This is inconsistent with our result. Therefore, to reproduce the spectra of $2\nu_Q$ and $3\nu_Q$ simultaneously, the peak-shift was simulated as a function of the internal magnetic field (H_{int}) and the angle θ between H_{int} and V_{zz} . The red curves in Fig. 3(b) show the calculated peak-frequencies

of $2\nu_Q$ and $3\nu_Q$ against H_{int} , assuming the appropriate angle $\theta = 88.3^\circ$. Here, the dark (light) tone on the colored curve represents the large (small) intensity expected in the spectrum. If θ were ~ 0 or much smaller than 90° , the $3\nu_Q$ spectrum would be largely split into two peaks, one of which should be observed at a higher frequency side than the frequency expected for zero H_{int} . However, in fact, no such higher frequency peak is detected, indicating that θ is close to 90° . The simulations are compared with the experiments for $2\nu_Q$ and $3\nu_Q$ in Figs. 3(c) and 3(d), respectively. As shown by the pink dashed curves, a small splitting and small shift to lower frequency observed for $3\nu_Q$ -peaks and a large splitting and large shift for $2\nu_Q$ -peaks are simultaneously reproduced by H_{int} with the largest weight ($\equiv H_{\text{int}}^{\text{peak}}$) ~ 0.18 T and $\theta \sim 88.3^\circ$. Here, a skew normal distribution of H_{int} shown in Fig. 3(e) was used, which is explained in detail in the Supplement(A). We have to consider not only the presence of above-mentioned La(2)_a sites with $H_{\text{int}} \neq 0$ (h_{a}^\pm) but also the presence of La(2)_a ones with $H_{\text{int}} = 0$ (h_{a}^0), where H_{int} is almost canceled out, as shown by the green dashed curves in Figs. 3(c) and 3(d). The volume fraction of La(2)_a with $H_{\text{int}} = 0$ [$V(h_{\text{a}}^0)$] is roughly comparable to that with $H_{\text{int}} \neq 0$ [$V(h_{\text{a}}^\pm)$]. The total calculated spectra shown by the red solid curves in Figs. 3(c) and 3(d) are superimposed by two comparable components for finite H_{int} (pink) and zero H_{int} (green) with $V(h_{\text{a}}^0)/V(h_{\text{a}}^\pm) \sim 0.5$. This result is consistently explained by the single spin-spinless stripe order model, as described later.

As for La(2)_b, the $3\nu_Q$ spectrum at ~ 16.2 MHz in Fig. 3(a) exhibits a large broadening and shift below T^* . The blue curves in Fig. 3(b) are the peak-shift simulation at $2\nu_Q$ and $3\nu_Q$ for La(2)_b as a function of H_{int} under the same $\theta (= 88.3^\circ)$ as that for La(2)_a. To explain the very broad spectrum from 15 to 16.5 MHz (see Fig. 3(f)), the H_{int} must be inhomogeneously enhanced at La(2)_b. In fact, the spectrum in Fig. 3(f) is well reproduced by the simulation (blue), assuming $H_{\text{int}}^{\text{peak}} \sim 0.44$ T and its skew normal distribution shown in Fig. 3(e). It is noteworthy that the La(2)_b site with $H_{\text{int}} = 0$ was not observed at ~ 16.2 MHz, as seen in Fig. 3(f), indicating that there are few or no La(2)_b sites with $H_{\text{int}} = 0$. In this context, it is reasonable to explain that the $2\nu_Q$ -spectrum of La(2)_b at ~ 10.6 MHz in Fig. 3(a) is undetectably small, which is due to a huge broadening and wide splitting by the broad distribution of $H_{\text{int}} = 0.2 \sim 0.5$ T, as expected by the simulation of Fig. 3(b). These features are quite different from those for La(2)_a. Since H_{int} is generally given by a product of $A_{\text{hf}}^{\text{a,b}}$ and the Ni moment (M_{Ni}), the difference in H_{int} for La(2)_{a,b} sites is attributed to the variation in A_{hf} and/or M_{Ni} . The experimentally obtained ratio $H_{\text{int}}^{\text{peak}}(b)/H_{\text{int}}^{\text{peak}}(a) \sim 2.44$ is quite similar to $|A_{\text{hf}}^b/A_{\text{hf}}^a| \sim 3.06$ obtained from the ratio of $(T_1T)^{-1}$. It is noteworthy that the magnitude of M_{Ni} on average does not change significantly around La(2)_a and La(2)_b, although the local defect is present near La(2)_b.

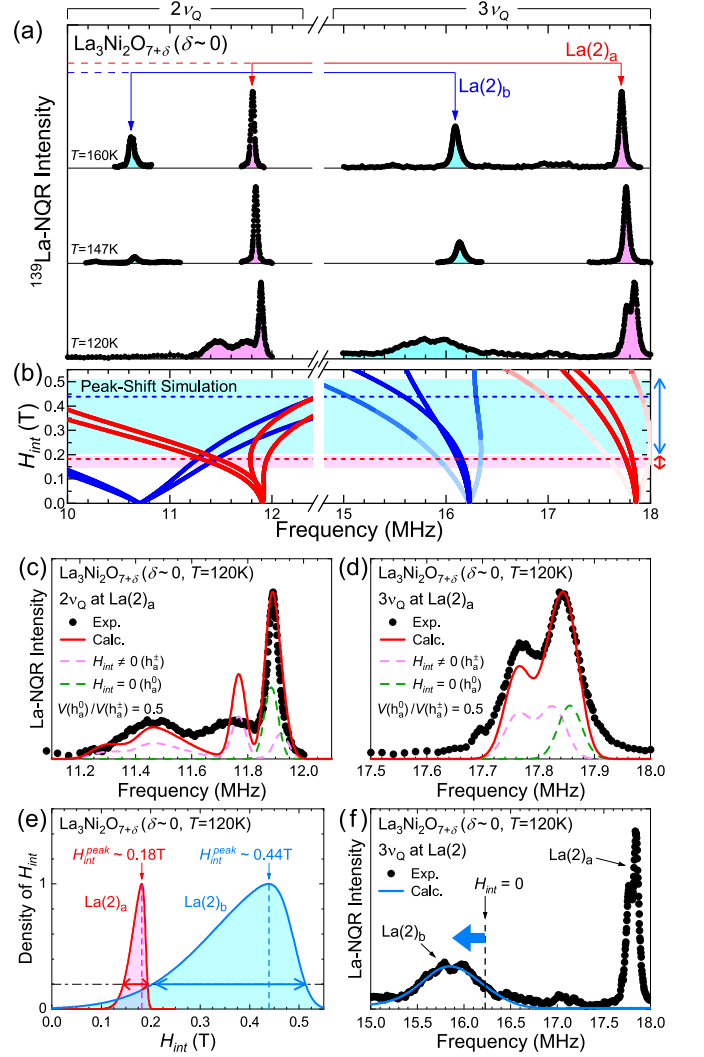


FIG. 3. (Color online) (a) La(2)-NQR spectra at $2\nu_Q$ (10 \sim 12 MHz) and $3\nu_Q$ (15 \sim 18 MHz) for La327 ($\delta \sim 0$) across T^* . (b) Simulation of peak frequencies as a function of H_{int} for La(2)_a (red) and La(2)_b (blue). (c) $2\nu_Q$ - and (d) $3\nu_Q$ -spectra for La(2)_a are roughly reproduced by the simulation (red line) superimposing two comparable components from the sites with finite H_{int} (pink dashed line) and zero H_{int} (green dashed line). The intensities of two components are divided by two for clarity. (e) Distributions of H_{int} used for the simulations in (c), (d), and (f), showing $H_{\text{int}}^{\text{peak}}$ and full width at 1/5 maximum for La(2)_a (red) and La(2)_b (blue). (f) The $3\nu_Q$ -spectrum of La(2)_b is reproduced only by the site with finite H_{int} (blue), indicating no peak of La(2)_b with $H_{\text{int}} = 0$.

4. Discussions

Figure 4(a) shows the illustration of the single spin-spinless stripe model, which is consistent with our NQR results. The M_{Ni} s are antiferromagnetically aligned in the ab -plane as $(\dots \uparrow \circ \downarrow \circ \uparrow \circ \dots)$ with the propagation vector $Q_{\text{SDW}} = (0, 1/2)$, as shown by the red and blue arrows in Fig. 4(a) (see also Supplement(B) for the simplest case without any O_{vac} s). This spin arrangement

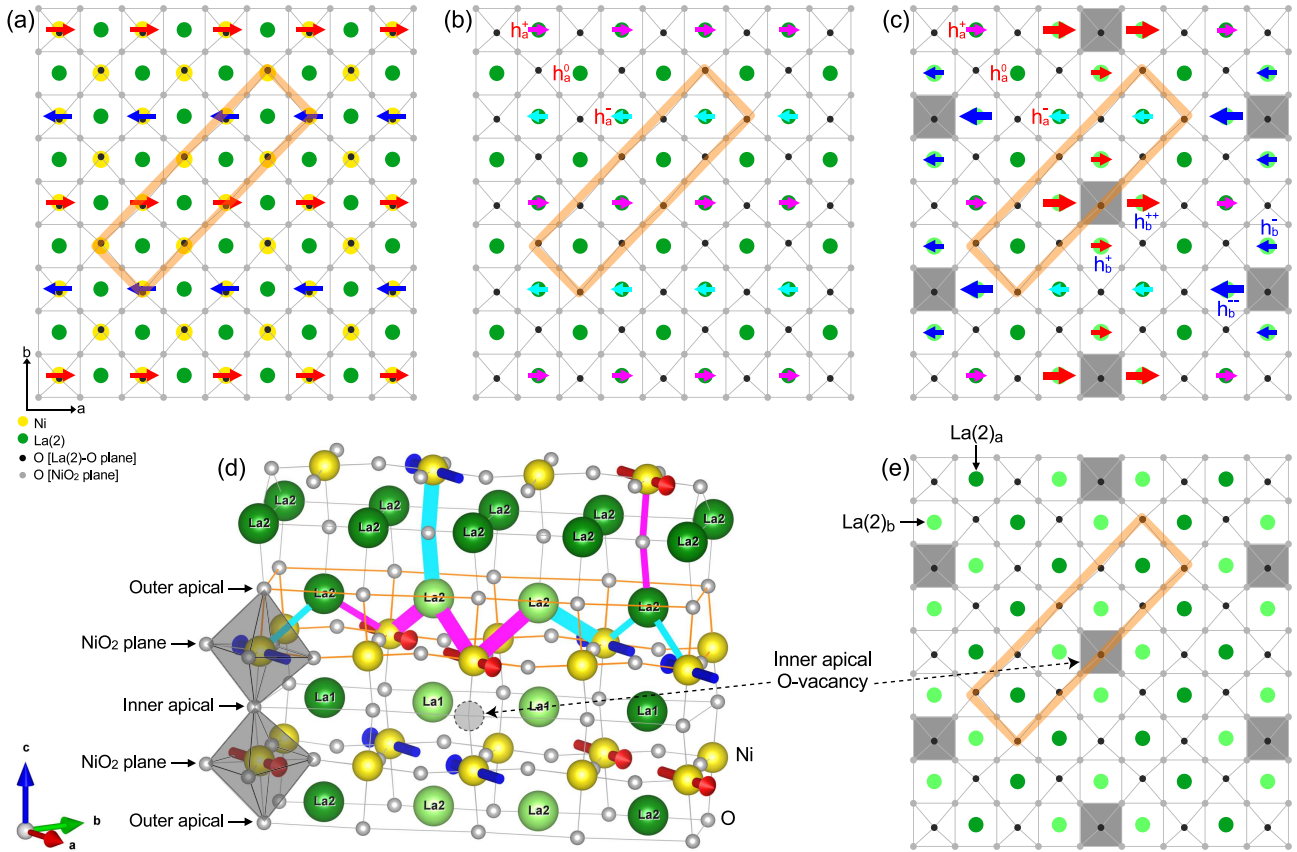


FIG. 4. (Color online) (a) Illustration of the single spin-spinless stripe order of M_{Ni} s (red/blue arrows) antiferromagnetically aligned within the NiO_2 layers, consistent with this study. The $La(2)$ - O plane is also projected onto this plane. (b) Spatial distribution of H_{int} at $La(2)_a$ of the ideal $La327$, derived from the spin configuration of (a). (c) $La(2)_b$ sites around O_{vac} s are dominated by inhomogeneously enhanced H_{int} (see arrows of different sizes). (d) Structure of $La327$ with Ni moments (red/blue arrows) corresponding to the area enclosed by the orange rectangle in (a). The light green $La(1)$ and $La(2)$ sites indicate the nearest neighbor sites of O_{vac} . (e) Spatial distribution of $La(2)_a$ (dark green) and $La(2)_b$ (light green) around O_{vac} s (gray) located on the Ni -spin channel above T^* , corresponding to (c) below T^* . The H_{int} at the $La(2)$ is either parallel or antiparallel to the direction of M_{Ni} in this model, which is determined by the properties of A_{hf} composed of transferred and/or dipolar fields. For the sake of simplicity, we temporarily draw the case dominated by the dipolar fields.

induces the comparable number of two $La(2)_a$ sites with $H_{int} = \pm 0.18$ and 0 T in the ab plane, corresponding to the h_a^\pm and h_a^0 sites on the straight Ni -spin and spinless channels, respectively, along the a -axis in Fig. 4(b). We consider that the most possible direction of M_{Ni} is along the a -axis: The direction of V_{zz} at $La(2)$ is tilted by about 6° from c - to b -axis in association with the tilt of the NiO_6 octahedron, as shown in Fig. 4(d), and thus θ should naturally be close to $\sim 84^\circ$ if assuming $M_{Ni} \parallel b$. However, the experimentally obtained θ ($\sim 88.3^\circ$) is very close to 90° , suggesting that the direction of M_{Ni} avoids the tilting direction of the octahedra (b -axis). We also exclude the cases of $M_{Ni} \parallel c$ and non-parallel to a -axis within the ab plane, because in such situations the h_a^0 site is eliminated.

Next we discuss the origin of the inhomogeneously enhanced H_{int} at the $La(2)_b$ site. As shown in Fig. 1, the spectral intensity for $La(2)_b$ is similar to that for $La(2)_a$ in the paramagnetic state above T^* for each $La327$ sample used in this study. If there is an O_{vac} at an inner

apical site, as shown in Fig. 4(e), the neighboring four (eight for upper and lower sites) $La(2)_a$ sites (dark green) are turned into $La(2)_b$ sites (light green). Thus, the number of $La(2)_b$ would be close to that of $La(2)_a$, assuming that the density of O_{vac} at the inner apical oxygen site is $\sim 1/8$ and that O_{vac} s are separated from each other beyond the distance of the second nearest neighbor. Such a hypothetical $La327$ ($\delta = 1/8$) crystal with inner apical O_{vac} s will induce the similar volume fraction for $La(2)_a$ and $La(2)_b$, which is consistent with this study. Considering this situation, as shown in Fig. 4(c), the nearest four (eight) $La(2)_b$ sites around O_{vac} s are further divided into two magnetically different sites below T^* , that is, the sites with strongly enhanced H_{int} ($\equiv h_b^{\pm\pm}$) and with moderate H_{int} ($\equiv h_b^\pm$), which appear on the Ni -spin and spinless channels around O_{vac} s, respectively. Even at the $La(2)_b$ site on the spinless channel, denoted as h_b^\pm , the hyperfine field from a Ni spin next to an O_{vac} is plausibly different from that from a Ni spin without any O_{vac} s, resulting in the imperfect cancellation of H_{int} from the sur-

rounding Ni spins. It gives a reasonable explanation for the experimental facts that the value of H_{int} at La(2)_b is inhomogeneously enhanced, and no La(2)_b site with $H_{\text{int}} = 0$, which are accounted for within the same model used for the La(2)_a site.

We address the feature of M_{Ni} for the intrinsic La(2)_a site. The H_{int} was evaluated to be ~ 0.18 T, which is one order smaller than ~ 2 T at the La site of La₂NiO₄ (La214) in the antiferromagnetic (AFM) order by large $M_{\text{Ni}}^{214} \sim 1.7 \mu_{\text{B}}$ corresponding to a high spin state of Ni²⁺ (d^8).^{27,28} Since A_{hf} is different from that of La214, it is difficult to estimate the exact M_{Ni} of La327 so far. However, at least the observation of the very small H_{int} in La327 suggests the significant reduction of M_{Ni} due to itinerant d -electrons in metallic La327, in contrast to the localized regime of insulating La214. According to the previous μSR experiment,¹⁵ $M_{\text{Ni}} \sim 0.42 \mu_{\text{B}}$ is anticipated if M_{Ni} is assumed to be within the ab plane. It is further supported by our experimental fact that M_{Ni} is along the a -axis. Such a reduction of M_{Ni} suggests that most of spins in the $d_{3z^2-r^2}$ -orbital may be canceled by forming a spin-singlet like state, since the bonding-orbital part of the $d_{3z^2-r^2}$ -band derived from the NiO₂ bilayers would be almost filled in La327.²⁹⁻³¹ Therefore, it is likely that the main amplitude of M_{Ni} originates from spins of the $d_{x^2-y^2}$ -band and the mixed band of $d_{3z^2-r^2}/x^2-y^2$. If assuming that most of M_{Ni} s would be derived only from spins in the nearly 1/4-filled $d_{x^2-y^2}$ -orbital, the maximum of M_{Ni} is expected to be about $0.5 \mu_{\text{B}}$, which is close to the M_{Ni} discussed above.

Finally, we note that the CDW order at the intrinsic La(2)_a site cannot be clearly detected from the current study in the measured T range from 100 to 300K. If the CDW order were present, it might be considerably weaker than the SDW order in this T range. Therefore we use the term "spin-spinless" rather than "spin-charge" to correctly express the current result in this paper. Our conclusion is different from the double spin stripe and double charge stripe order proposed microscopically by La(1)-NMR¹⁹ and La(2)-NQR³², respectively. In order to deduce the magnetic structure in La327, two conditions must be satisfied, namely the existence of the h_{a}^0 site and the direction of H_{int} parallel to the a -axis. As shown in Fig. 4(d), the La(2) site is surrounded by four first-nearest-neighbor Ni sites obliquely below La(2) and one second-nearest-neighbor Ni site above La(2). If the second-nearest-neighbor Ni site is not spinless, the cancellation of H_{int} at the La(2) becomes extremely difficult. Thus, the presence of the Ni-spinless channel is probably indispensable to explain the appearance of the h_{a}^0 site in the SDW order. Furthermore, a local symmetric spin configuration of four first-nearest-neighbor Ni

sites around La(2) is required for the good cancellation of H_{int} . However, in the cases of the double spin stripe and double spin-charge stripe models, it is very difficult to obtain the innegligible amount of h_{a}^0 sites due to the low local symmetry of the spin configuration around the La(2) site. As for the direction of H_{int} in these double stripe systems, it should be fairly tilted from the ab -plane to the c -axis in many conditions, which is inconsistent with our NQR result. Regarding to the single spin-spinless stripe structure, our NQR result is almost consistent with the RIXS,¹¹ μSR ,¹⁵ and RXS¹⁷ studies. The large reduction of M_{Ni} in La327 deduced from the present NQR study is reasonably consistent with the undetectably small moment suggested by the neutron scattering experiment²⁰. In addition, our NQR result is in good agreement with the spatial arrangement in which inner apical O_{vac}s are located on the Ni-spin channel, not on the Ni-spinless channel (see the detail in Supplement(C)), indicating that the location of inner apical O_{vac}s may not be completely random. If inner apical O_{vac}s form such a pattern as the stripe, it is of interest in terms of how the pattern of O_{vac}s affects the SDW order at low pressure and the superconductivity at high pressure.

5. Conclusions

In summary, the ¹³⁹La(2)-NQR measurement in La327 revealed the appearance of two intrinsic La(2)_a sites with zero and finite H_{int} s below $T^* \sim 150\text{K}$, which is consistently explained by the single spin-spinless stripe order model with the moderately reduced $M_{\text{Ni}}^{327} \parallel a$ that is antiferromagnetically aligned by $Q_{\text{SDW}} = (0, 1/2)$. Even for the La(2)_b site close to inner apical O_{vac}s, these NQR results are mostly explained within the same model by considering inhomogeneous H_{int} enhanced around O_{vac}s. These results provide further insight into understanding the relationship with the high- T_c states at high pressure.

Acknowledgments

This work was partially supported by the Takahashi Industrial and Economic Research Foundation and JSPS KAKENHI Grant No. JP24K01333. One of the authors (M. K.) was supported by JST SPRING, Grant No. JPMJSP2138 and by Kato Foundation for Promotion of Science, Grant No. KS-3614. Two of the authors (H. S. and Y. T.) were supported by World Premier International Research Center Initiative (WPI), MEXT, Japan, Grant No. JPMJSP2138.

¹ H. Sun, M. Huo, X. Hu, J. Li, Z. Liu, Y. Han, L. Tang, Z. Mao, P. Yang, B. Wang, J. Cheng, D.-X. Yao, G.-M.

Zhang, and M. Wang, Nature **621**, 493 (2023).

- ² J. Hou, P.-T. Yang, Z.-Y. Liu, J.-Y. Li, P.-F. Shan, L. Ma, G. Wang, N.-N. Wang, H.-Z. Guo, J.-P. Sun, Y. Uwatoko, M. Wang, G.-M. Zhang, B.-S. Wang, and J.-G. Cheng, *Chin. Phys. Lett.* **40**, 117302 (2023).
- ³ Y. Zhang, D. Su, Y. Huang, Z. Shan, H. Sun, M. Huo, K. Ye, J. Zhang, Z. Yang, Y. Xu, Y. Su, R. Li, M. Smidman, M. Wang, L. Jiao, and H. Yuan, *Nat. Phys.* **20**, 1269 (2024).
- ⁴ G. Wang, N. N. Wang, X. L. Shen, J. Hou, L. Ma, L. F. Shi, Z. A. Ren, Y. D. Gu, H. M. Ma, P. T. Yang, Z. Y. Liu, H. Z. Guo, J. P. Sun, G. M. Zhang, S. Calder, J.-Q. Yan, B. S. Wang, Y. Uwatoko, and J.-G. Cheng, *Phys. Rev. X* **14**, 011040 (2024).
- ⁵ N. N. Wang, G. Wang, X. L. Shen, J. Hou, J. Luo, X. P. Ma, H. X. Yang, L. F. Shi, J. Dou, J. Feng, J. Yang, Y. Q. Shi, Z. A. Ren, H. M. Ma, P. T. Yang, Z. Y. Liu, Y. Liu, H. Zhang, X. L. Dong, Y. X. Wang, K. Jiang, J. P. Hu, S. Nagasaki, K. Kitagawa, S. Calder, J. Q. Yan, J. P. Sun, B. S. Wang, R. Zhou, Y. Uwatoko, and J. G. Cheng, *Nature* **634**, 579 (2024).
- ⁶ E. K. Ko, Y. Yu, Y. Liu, L. Bhatt, J. Li, V. Thampy, C.-T. Kuo, B. Y. Wang, Y. Lee, K. Lee, J.-S. Lee, B. H. Goodge, D. A. Muller, and H. Y. Hwang, *Nature* (2024), 10.1038/s41586-024-08525-3.
- ⁷ Z. Zhang, M. Greenblatt, and J. B. Goodenough, *J. Solid State Chem.* **108**, 402 (1994).
- ⁸ G. Q. Wu, J. J. Neumeier, and M. F. Hundley, *Phys. Rev. B* **63**, 245120 (2001).
- ⁹ Z. Liu, H. Sun, M. Huo, X. Ma, Y. Ji, E. Yi, L. Li, H. Liu, J. Yu, Z. Zhang, Z. Chen, F. Liang, H. Dong, H. Guo, D. Zhong, B. Shen, S. Li, and M. Wang, *Sci. China: Phys. Mech. Astron.* **66**, 217411 (2023).
- ¹⁰ Z. Liu, M. Huo, J. Li, Q. Li, Y. Liu, Y. Dai, X. Zhou, J. Hao, Y. Lu, M. Wang, and H.-H. Wen, *Nat. Comm.* **15**, 7570 (2024).
- ¹¹ X. Chen, J. Choi, Z. Jiang, J. Mei, K. Jiang, J. Li, S. Agrestini, M. Garcia-Fernandez, X. Huang, H. Sun, D. Shen, M. Wang, J. Hu, Y. Lu, K.-J. Zhou, and D. Feng, *Nat. Commun.* **15**, 9597 (2024).
- ¹² S. Taniguchi, T. Nishikawa, Y. Yasui, Y. Kobayashi, J. Takeda, S. Shamoto and M. Sato, *J. Phys. Soc. Jpn.* **64**, 1644 (1995).
- ¹³ M. Kakoi, T. Oi, Y. Ohshita, M. Yashima, K. Kuroki, T. Kato, H. Takahashi, S. Ishiwata, Y. Adachi, N. Hatada, T. Uda, and H. Mukuda, *J. Phys. Soc. Jpn.* **93**, 053702 (2024).
- ¹⁴ Y. Meng, Y. Yang, H. Sun, S. Zhang, J. Luo, L. Chen, X. Ma, M. Wang, F. Hong, X. Wang, and X. Yu, *Nat. Commun.* **15**, 10408 (2024).
- ¹⁵ K. Chen, X. Liu, J. Jiao, M. Zou, Y. Luo, Q. Wu, N. Zhang, Y. Guo, and L. Shu, *Phys. Rev. Lett.* **132**, 256503 (2024).
- ¹⁶ R. Khasanov, T. J. Hicken, D. J. Gawryluk, L. P. Sorel, S. Bötzel, F. Lechermann, I. M. Eremin, H. Luetkens, and Z. Guguchia, *Nat. Phys.* (2025), in press..
- ¹⁷ X. Ren, R. Sutarto, X. Wu, J. Zhang, H. Huang, T. Xiang, J. Hu, R. Comin, X. Zhou, and Z. Zhu, *Commun. Phys.* **8**, 52 (2025).
- ¹⁸ N. K Gupta, R. Gong, Y. Wu, M. Kang, C. T. Parzyck, B. Z. Gregory, N. Costa, R. Sutarto, S. Sarker, A. Singer, D. G. Schlom, K. M. Shen, and D. G. Hawthorn, *arXiv:2409.03210*.
- ¹⁹ D. Zhao, Y. Zhou, M. Huo, Y. Wang, L. Nie, Y. Yang, J. Ying, M. Wang, T. Wu, and X. Chen, *Sci. Bull.* (2025) in press.
- ²⁰ T. Xie, M. Huo, X. Ni, F. Shen, X. Huang, H. Sun, H. C. Walker, D. Adroja, D. Yu, B. Shen, L. He, K. Cao, and M. Wang, *Sci. Bull.* **69**, 3221 (2024).
- ²¹ T. Fukamachi, K. Oda, Y. Kobayashi, T. Miyashita, and M. Sato, *J. Phys. Soc. Jpn.* **70**, 2757 (2001).
- ²² Y. Ueki, H. Sakurai, H. Nagata, K. Yamane, R. Matsumoto, K. Terashima, K. Hirose, H. Ohta, M. Kato, and Y. Takano, *J. Phys. Soc. Jpn.* **94**, 013703 (2025).
- ²³ Y. Adachi, N. Hatada, K. Hirota, M. Kato, and T. Uda, *J. Am. Ceram. Soc.* **102**, 7077 (2019).
- ²⁴ H. Nagata, H. Sakurai, Y. Ueki, K. Yamane, R. Matsumoto, K. Terashima, K. Hirose, H. Ohta, M. Kato, and Y. Takano, *J. Phys. Soc. Jpn.* **93**, 095003 (2024).
- ²⁵ D. E. Maclaughlin, J. D. Williamson, and J. Butterworth, *Phys. Rev. B* **4**, 60 (1971).
- ²⁶ Z. Dong, M. Huo, J. Li, J. Li, P. Li, H. Sun, Y. Lu, M. Wang, Y. Wang, and Z. Chen, *Nature* **630**, 847 (2024).
- ²⁷ J. Rodriguez-Carvajal, M. T. Fernandez-Diaz, and J. L. Martinez, *J. Phys.: Condens. Matter* **3**, 3215 (1991).
- ²⁸ S. Wada, Y. Furukawa, M. Kaburagi, T. Kajitani, S. Hosoya, and Y. Yamada, *J. Phys.: Condens. Matter* **5**, 765 (1993).
- ²⁹ H. Sakakibara, N. Kitamine, M. Ochi, and K. Kuroki, *Phys. Rev. Lett.* **132**, 106002 (2024).
- ³⁰ Z. Luo, X. Hu, M. Wang, W. Wu, and D.-X. Yao, *Phys. Rev. Lett.* **131**, 126001 (2023).
- ³¹ Y. F. Yang, G. M. Zhang, and F. C. Zhang, *Phys. Rev. B* **108**, L140505 (2023).
- ³² J. Luo, J. Feng, G. Wang, N. N. Wang, J. Dou, A. F. Fang, J. Yang, J. G. Cheng, G. Q. Zheng, and R. Zhou, *arXiv:2501.11248*.

Supplement

A. Skew normal distribution used for the simulation of the asymmetric spectra

In this simulation, the spectral components with H_{int} at $2\nu_Q$ and $3\nu_Q$ are calculated using the skew (asymmetric) normal distribution shown in Fig. 3(e). The skew normal distribution $S(x, \xi, \sigma, \alpha)$ is expressed with a complementary error function $\text{erfc}(x)$ by

$$S(x, \xi, \sigma, \alpha) = \exp\left[-\left(\frac{x - \xi}{\sigma}\right)^2\right] \cdot \text{erfc}\left(-\alpha \frac{x - \xi}{\sigma}\right),$$

where ξ , σ and α are a mean, a standard deviation of the distribution, and a shape parameter of the asymmetry of the distribution, respectively. This function with $\alpha = 0$ is the same as the Gaussian (normal distribution) function. As for $\text{La}(2)_a$, the calculated $2\nu_Q$ and $3\nu_Q$ spectra in Figs. 3(c) and 3(d) are simultaneously reproduced with the same parameters $(\xi, \sigma, \alpha) = (0.19 \text{ T}, 0.035 \text{ T}, -6)$, respectively. The distribution of H_{int} is shown by the red curve in Fig. 3(e). The peak position of this asymmetric H_{int} distribution ($H_{\text{int}}^{\text{peak}}$) is $\sim 0.18 \text{ T}$. As for the $\text{La}(2)_b$ site, the calculated spectrum (blue solid line in Fig. 3(f)) is reproduced by applying the parameters of the H_{int} distribution $(\xi, \sigma, \alpha) = (0.49 \text{ T}, 0.22 \text{ T}, -6)$. This gives $H_{\text{int}}^{\text{peak}}$ (b) $\sim 0.44 \text{ T}$. The distribution of H_{int} is shown by the blue curve in Fig. 3(e). Both the amplitude and the distribution width of H_{int} for $\text{La}(2)_b$ are much larger than those for $\text{La}(2)_a$.

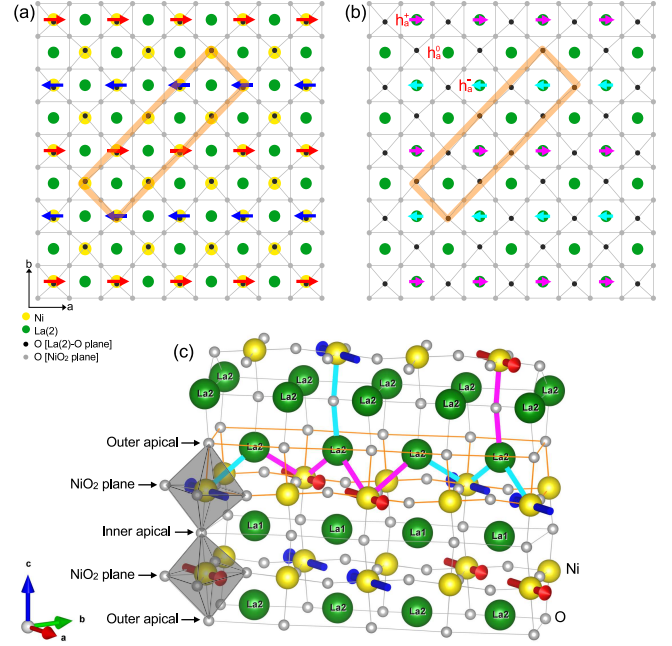
B. Single spin-spinless stripe order model : The simplest case for perfect crystal without any O_{vac} s

FIG. S1. (Color online) Single spin-spinless stripe order model for the simplest case in the perfect crystal without any O_{vac} s. (a) Illustration of the single spin-spinless stripe configuration of M_{Ni} s (red and blue arrows) antiferromagnetically aligned within the NiO_2 layers, consistent with this study. The $\text{La}(2)\text{-O}$ plane is also projected onto this plane. (b) Spatial distribution of H_{int} at the $\text{La}(2)_a$ site of the ideal $\text{La}327$, derived from the spin configuration shown in (a). Almost half of the intrinsic $\text{La}(2)_a$ sites are dominated by a finite H_{int} within the ab plane, while the other half are dominated by zero H_{int} . (c) Crystal structure of $\text{La}327$ including no O_{vac} s with M_{Ni} s (red and blue arrows). As for the direction of H_{int} at the $\text{La}(2)$ site, for the sake of simplicity, we temporarily draw the case where the dipolar fields are predominant.

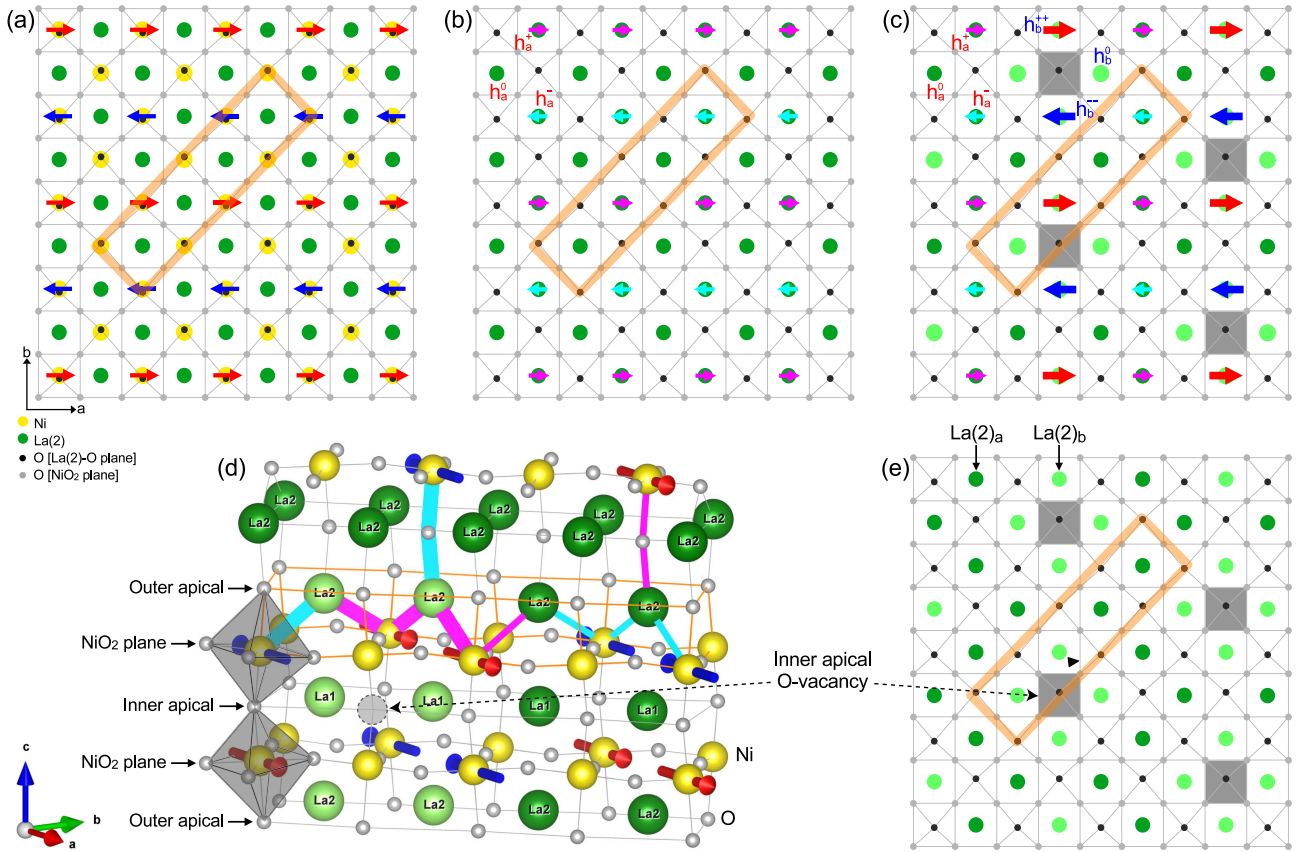


FIG. S2. (Color online) (a) Illustration of the single spin-spinless stripe order of M_{NiS} (red/blue arrows) antiferromagnetically aligned within the NiO_2 layers, consistent with this study. The $La(2)-O$ plane is also projected onto this plane. (b) Spatial distribution of H_{int} at $La(2)_a$ of the ideal La_{327} , derived from the spin configuration of (a). (c) $La(2)_b$ sites around O_{vac} s are dominated by the enhanced H_{int} (see arrows of different sizes). (d) Structure of La_{327} with Ni moments (red/blue arrows) corresponding to the area enclosed by the orange rectangle in (a). The light green $La(1)$ and $La(2)$ sites indicate the nearest neighbor sites of O_{vac} . (e) Spatial distribution of $La(2)_a$ (dark green) and $La(2)_b$ (light green) around O_{vac} s (gray) on the Ni -spinless channel above T^* , corresponding to (c) below T^* . The H_{int} at the $La(2)$ is either parallel or antiparallel to the direction of M_{Ni} in this model, which is determined by the properties of the A_{hf} composed of transferred and/or dipolar fields. We temporarily draw the case dominated by the dipolar fields for simplicity.

C. Influence of relative positional differences between the inner apical O_{vac} site and Ni -spin/spinless channels

Here we comment on the reason why we adopt the scenario that the inner apical O_{vac} site is located on the Ni -spin channel in Fig. 4. In order to obtain such a conclusion, we also consider the another possibility that inner apical O_{vac} s are located on the Ni -spinless channels. It is possible that an O_{vac} can randomly come into any inner apical oxygen sites. Figure S2(e) shows the case where all inner apical O_{vac} s are on the Ni -spinless channels. In this case, H_{int} is canceled on the Ni -spinless

channel even at the $La(2)_b$ site. This is not consistent with the present NQR result, where there are few or no $La(2)_b$ sites with $H_{int} = 0$. Therefore, most of inner apical O_{vac} s are likely located on the Ni -spin channel. These results suggest that O_{vac} s may also form a stripe pattern like the Ni -spin/spinless channels. Ni spins are induced on the channel with higher oxygen deficiency, corresponding to the Ni -spin channel. On the other hand, no Ni spins are induced in the channel with almost no oxygen deficiency, corresponding to the Ni -spinless channel. It is of interest in terms of how the possible spatial pattern of O_{vac} s affects the SDW order at low pressure and the superconductivity at high pressure.